Spectral anisotropy in forced two-dimensional turbulence on a rotating sphere

Toru Nozawa[a] and Shigeo Yoden[b]
Department of Geophysics, Kyoto University, Kyoto 606-01, Japan

(Received 30 July 1996; accepted 18 August 1997)

The datasets on the forced two-dimensional turbulence on a rotating sphere obtained in our recent direct numerical simulations were analyzed to study the spectral anisotropy due to the rotation of the sphere. The results were also compared with those previously obtained in some β-plane experiments to assess the β-plane approximation of the rotating sphere. Owing to the effect of rotation the upward energy cascade ceases around a characteristic total wavenumber n_β at which the linear ''β-term'' is comparable to the nonlinear Jacobian term. The energy density of zonal components ($m=0$) is dominant in the range of $n \lesssim n_\beta$ while the energy is very small in an airfoil-shaped region at the lower edge in the wavenumber space (m,n). Anisotropic distribution of the energy is also found in the high wavenumber region $n \gtrsim n_\beta$; the energy density decreases as the zonal wavenumber m increases. The flow field in the spherical geometry is projected on some tangential planes from the equator to the poles to compare the spherical results directory with previous β-plane experiments. The energy distribution becomes anisotropic to have dominant zonal components as the local ''β-effect'' increases (or the tangential plane is put closer to the equator). In the case on equatorial tangential planes, the region in which the energy density is very small shows a dumbbell shape indicating strong anisotropy; this is the first confirmation of the recent finding by Vallis and Maltrud in full spherical geometry. © *1997 American Institute of Physics.*
[S1070-6631(97)02812-2]

I. INTRODUCTION

As a geophysical application of the two-dimensional (2D) turbulence theory,[1–3] Rhines[4] first studied on the decaying 2D turbulence on a β-plane. He showed that the reverse energy cascade is arrested roughly at a characteristic wavenumber $k_\beta=\sqrt{\beta/2U}$, where U is the r.m.s. velocity and β the meridional gradient of the Coriolis parameter f. He also pointed out the emergence of a zonal band structure due to the β-effect. On the subject of the spectral anisotropy, Vallis and Maltrud[5] (hereafter referred to as VM) recently proposed a couple of transition curves from turbulent motion to wave-like behavior; one of them is the ''wave-turbulence boundary'' obtained by equating the reciprocal of the eddy turnover time with the Rossby wave frequency. The curve of this boundary exhibits a characteristic dumbbell shape in the 2D wavenumber space (k,l), and the 2D energy spectral density in their experiments with high-wavenumber forcing[6] shows a qualitatively similar dumbbell shape. In addition to these studies, some numerical experiments on the 2D turbulence on a β-plane have been done to investigate the effect of the rotation of planets.[7–9]

The β-plane is an approximation of a longitudinal band of the rotating sphere. The latitudinal variation of β arising from the sphericity is set to zero, and usually infiniteness of the domain is assumed by using a cyclic boundary condition.

As for the spherical geometry, Nozawa and Yoden[10] (referred to as NY) did numerical experiments on the forced 2D turbulence on a rotating sphere aiming at a methodical sweep in parameter space; the sensitivity of pattern formation to the rotation rate and the forcing wavenumber was investigated. A zonal band structure which consists of alternating easterly and westerly jets emerges owing to the effect of rotation as in Williams.[11] When the forcing wavenumber is small and the rotation rate is large, the band structure is confined in high latitudes as in the decaying case.[12] In these studies in the spherical geometry, however, the spectral anisotropy has not been investigated very much.

In this paper, by using the datasets obtained in NY, we examine the spectral anisotropy in the forced 2D turbulence on a rotating sphere and assess the validity of the previous results obtained in the β-plane studies. Taking advantage of the high-resolution numerical model, the 2D energy density is also calculated for a square region of the flow fields that are orthographically projected on some tangential planes of different latitudes. The validity of the β-plane studies is assessed by comparing the 2D energy density on the tangential plane to that obtained in VM. Although a large part of the results here has already been reported in the β-plane studies, this is the first attempt to validate the nature of the β-plane 2D turbulence by the direct numerical simulation in a full spherical geometry. The numerical experiment is described in section II, and results are given in section III. A discussion is given in section IV, and conclusions are in section V.

II. NUMERICAL EXPERIMENT

The governing equation used in NY is the vorticity equation for 2D nondivergent flow on a rotating sphere:

[a]Corresponding author. Current address: Disaster Prevention Research Institute, Kyoto University, Kyoto 611, Japan; Telephone: +81-774-38-4159; Fax: +81-774-33-0026; Electronic mail: nozawa@bouhuu.dpri.kyoto-u.ac.jp
[b]Electronic mail: yoden@kugi.kyoto-u.ac.jp

 1070-6631/97/9(12)/3834/9/$10.00

TABLE I. Summary of experiments. The column headings are given in the text.

Series	Run #	n_f	Ω/Ω_J	Group	$\overline{U}$ (ms^{-1})	n_β	k_β $\varphi_c=0°$	k_β $\varphi_c=\pm45°$
I	1	20	0.00	**A**	66.9	⋯	⋯	⋯
	2		0.25	**B**	65.1	7.23	1.170	0.961
	3		0.50	**B**	63.9	10.32	1.949	1.307
	4		1.00	**C**	56.5	15.53	3.198	1.971
	5		2.00	**C**	40.0	26.09	5.310	3.654
	6		4.00	**C**	27.3	44.69	9.839	6.777
II	7	40	0.00	**A**	67.1	⋯	⋯	⋯
	8		0.25	**B**	68.0	7.07	1.236	0.938
	9		0.50	**B**	67.0	10.08	1.926	1.298
	10		1.00	**B**	63.3	14.66	2.485	1.903
	11		2.00	**B**	59.9	21.32	3.898	2.751
	12		4.00	**C**	43.2	35.51	7.688	4.465
III	13	79	0.00	**A**	67.0	⋯	⋯	⋯
	14		0.25	**B**	68.6	7.04	1.222	0.925
	15		0.50	**B**	68.0	10.00	1.750	1.306
	16		1.00	**B**	68.5	14.09	2.676	1.941
	17		2.00	**B**	62.9	20.81	3.472	2.793
	18		4.00	**B**	55.9	31.20	5.143	4.138

$$\frac{\partial\zeta}{\partial t}+\frac{1}{a^2}J(\psi,\zeta)+\frac{2\Omega}{a^2}\frac{\partial\psi}{\partial\lambda}=F+\nu\left(\nabla^2+\frac{2}{a^2}\right)\zeta, \tag{1}$$

where $\psi(\lambda,\mu,t)$ is a streamfunction field, $\zeta(\lambda,\mu,t)=\nabla^2\psi$: vorticity, λ: longitude, μ: sine latitude, t: time, ∇^2: horizontal Laplacian, $J(\psi,\zeta)$: horizontal Jacobian, a: radius of the sphere, Ω: rotation rate of the sphere, ν: kinematic viscosity coefficient, and $F(\lambda,\mu,t)$: vorticity forcing function. The radius and the rotation rate of the sphere are set to those of Jupiter, and the time t is measured by the Jovian day. The forcing F is a random stirring at a narrow wavenumber range of $n_f-\Delta n\leqslant n\leqslant n_f+\Delta n$ with $\Delta n=2$. Equation (1) was integrated using a pseudospectral method with a triangular truncation of $N=199$; grid points for the spectral transformation are 600 (longitude) $\times$ 300 (latitude). Time integrations were done for 1000 J.days from an initial condition of zero velocity field (see NY for details).

Table I gives a summary of the eighteen experiments done in NY. For the series I, II, and III experiments, the forcing wavenumber is chosen as $n_f=20$, 40, and 79, respectively. For each forcing wavenumber, six values of the rotation rate are chosen: $\Omega/\Omega_J=0.00$, 0.25, 0.50, 1.00, 2.00, and 4.00, where Ω_J is the rotation rate of Jupiter. Based on the obtained zonal band structure, each run was classified into three groups, **A**, **B**, and **C** in NY.

Figure 1 shows the time-averaged zonal mean zonal angular momentum $\overline{[M]}\equiv a\sqrt{1-\mu^2}\,\overline{[u]}$ (broken line), zonal mean potential vorticity $\overline{[q]}\equiv\overline{[\zeta]}+2\Omega\mu$ (dot–dashed line), and meridional gradient of the zonal mean potential vorticity $\overline{[q]}_y\equiv(\sqrt{1-\mu^2}/a)(\partial\overline{[q]}/\partial\mu)$ (solid line) for three typical runs of #7 (group **A**), #10 (group **B**), and #12 (group **C**) in series II, where $u(\lambda,\mu,t)\equiv-(\sqrt{1-\mu^2}/a)(\partial\psi/\partial\mu)$ is a zonal velocity, and $[\cdots]$ denotes the zonal mean. An overbar indicates the time average from 800 to 1000 J.days. In group **A** with $\Omega=0$, the easterly or westerly flow dominates over a hemisphere (a). The zonal mean potential vorticity and its meridional gradient is very small in all the latitudes. In group **B**, the alternating easterly and westerly zonal band structure emerges in all the latitudes (b). However, the zonal mean potential vorticity $\overline{[q]}$ increases with μ monotonously, because the planetary vorticity $2\Omega\mu$ is dominant. Therefore, $\overline{[q]}_y$ is positive in all the latitudes indicating that the jets are barotropically stable. The meridional gradient of the zonal mean potential vorticity largely deviates from that of the planetary vorticity $(2\Omega/a)\sqrt{1-\mu^2}$ (thin dotted line), and this deviation corresponds to a curvature of the mean zonal angular momentum $\overline{[M]}$. Thus the westerly jet is narrow and steep while the easterly is broad and gentle. In group **C**, the circumpolar easterly jet appears in high latitudes and weak zonal flow in middle and low latitudes (c). The meridional gradient of $\overline{[q]}$ is nearly equal to that of the planetary vorticity in the middle and low latitudes (outside of the circum-

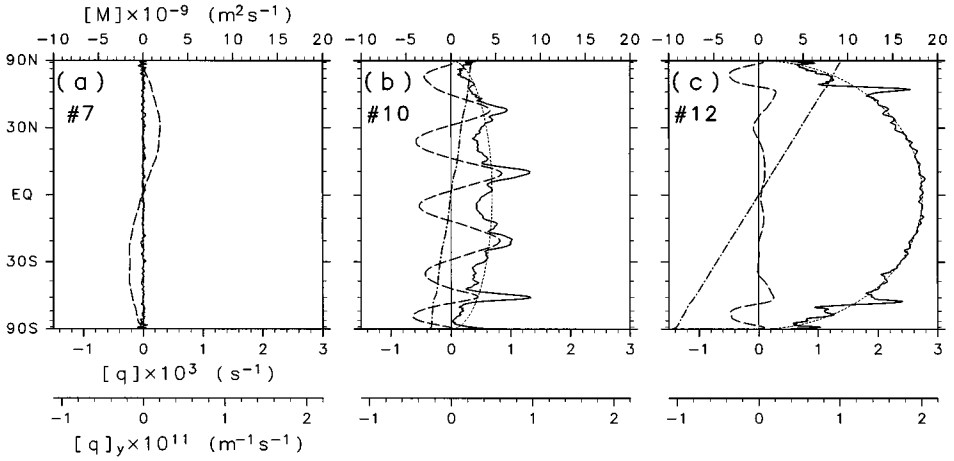

FIG. 1. Meridional distributions of zonal-mean zonal angular momentum (broken line), zonal-mean potential vorticity (dot-dashed line), meridional gradient of zonal-mean potential vorticity (solid line), and that of the planetary vorticity (thin dotted line) for three typical runs of (a) #7, (b) #10, and (c) #12 in series II. Averaged time is from 800 to 1000 J.days.

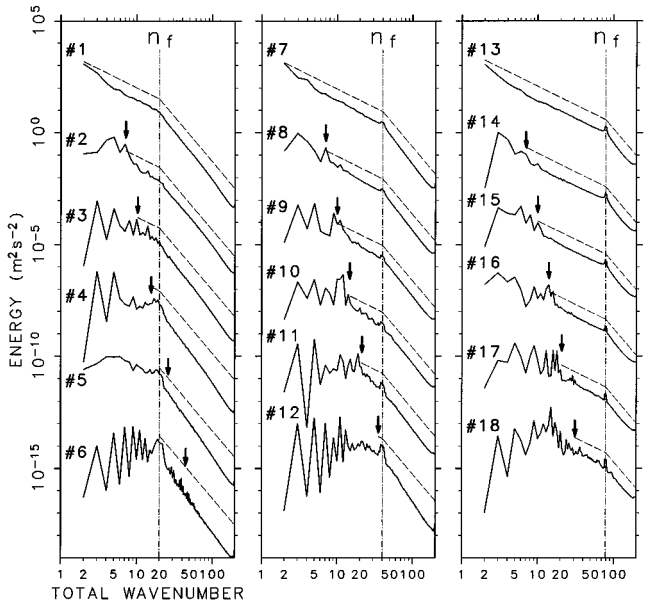

FIG. 2. Energy spectrum averaged from 800 to 1000 J.days. The number in the upper left of each curve represents the run number. The curves are arranged from left to right in the order of the forcing wavenumber n_f, and from top to bottom in the order of the rotation rate Ω/Ω_J; each spectrum is successively shifted down by a factor of 10^{-3} m^2 s^{-2} for clarity. Thin dot-dashed lines represent the forcing wavenumber n_f and thick arrows the wavenumber n_β at which scale the ''β-term'' is comparable to the nonlinear Jacobian term. A broken line of n^{-4} is added in the range of $n_f \leqslant n \leqslant N = 199$ for all runs. Another broken line of $n^{-5/3}$ is also added in the range of $n_\beta \leqslant n \leqslant n_f$ except for the two runs of #5 and #6.

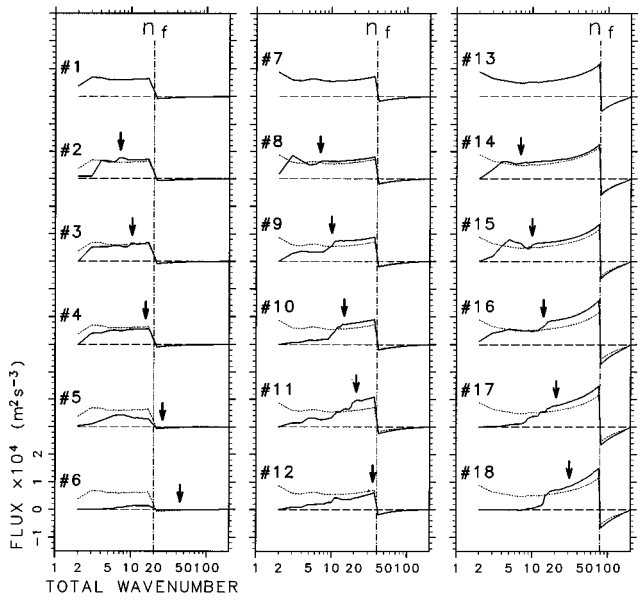

FIG. 3. Time-averaged energy flux function for the last 200 J.days. Broken lines are zero lines. The wavenumbers n_f (thin dot–dashed lines) and n_β (thick arrows) are the same as in Fig. 2. Arrangement of the curves is identical to that of the curves in Fig. 2. The energy flux function for the run without rotation (top curves in each panel) is superimposed on that for the other runs in the same series (thin dotted lines).

polar easterly jets), while it becomes nearly constant in high latitudes. A large gap of $\overline{[q]}_y$ exists around $\varphi \sim \pm 55°$.

III. RESULTS

A. Energy spectrum on a sphere

Figure 2 shows the time-averaged energy spectrum $\overline{E}(n)$:

$$\overline{E}(n) = \frac{1}{2}\frac{n(n+1)}{a^2}\sum_{m=-n}^{n}\overline{|\psi_n^m(t)|^2}, \tag{2}$$

where $\psi_n^m(t)$ is an expansion coefficient of ψ with spherical harmonics $Y_n^m(\lambda,\mu)$:

$$\psi(\lambda,\mu,t) = \sum_{n=2}^{N}\sum_{m=-n}^{n}\psi_n^m(t)Y_n^m(\lambda,\mu). \tag{3}$$

For all the experiments, the slope of the energy spectrum is close to n^{-4} in the enstrophy-cascading range of $n \gtrsim n_f$. When the forcing wavenumber is not large (series I and II), however, the slope in this range becomes a little steep as the rotation rate increases. An upward energy-cascading range is also obtained for the runs in groups **A** and **B**. The energy spectra are nearly proportional to $n^{-5/3}$ in this range, and the slope steepens slightly as Ω increases. In the case of no rotation (#1, #7, and #13; group **A**), the energy spectrum is steeper than $n^{-5/3}$ at the low wavenumbers of $n \lesssim 7$ because the energy is accumulating in this range owing to the finiteness of the spherical domain. For the experiments with rotation, on the other hand, the spectrum does not obey the power law of $n^{-5/3}$ at low wavenumbers; the energy-cascading range becomes narrow and the spectrum in this range becomes noisy as Ω increases.

A characteristic wavenumber n_β is also listed in Table I, which was defined in NY as

$$n_\beta \equiv a\sqrt{\langle\beta\rangle/(2\overline{U})}, \tag{4}$$

where $\overline{U}$ is the r.m.s. velocity averaged from 800 to 1000 J.days, and $\langle\beta\rangle$ is the spherical average of β: $\langle\beta\rangle = \pi\Omega/(2a)$. Figure 2 shows that n_β (indicated by an arrow) roughly gives the lower bound of the energy-cascading range. The spectrum does not show any clear power law in $2 \leqslant n \lesssim n_\beta$, where the linear ''$\beta$-term'' is larger than the nonlinear term in Eq. (1). When the forcing wavenumber is small and the rotation rate is large (#4–6, and #12; group **C**), the wavenumber n_β is nearly equal to or larger than n_f, and the energy-cascading range with an $n^{-5/3}$ power law is not found at all.

The energy flux functions for all runs are shown in Fig. 3. The energy flux function $\overline{\Pi}(n)$ is calculated from the energy transfer function $\overline{T}(n)$:

$$\overline{\Pi}(n) = \sum_{n'=2}^{n}\overline{T}(n'), \tag{5}$$

$$\overline{T}(n) = -\sum_{m=-n}^{n}\overline{\{\psi_n^m(t)\}^\dagger N_n^m(t)}, \tag{6}$$

where $N_n^m(t)$ is the expansion coefficient of the nonlinear Jacobian term, and $(\cdots)^\dagger$ denotes the complex conjugate. In the case of no rotation (group **A**), the energy flux is nearly constant in the range of $2 \leqslant n \lesssim n_f$, indicating that the energy

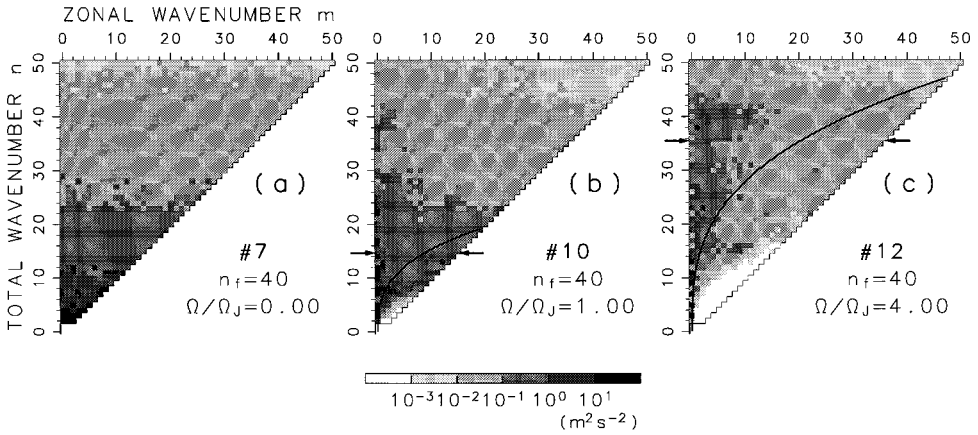

FIG. 4. Two-dimensional energy density averaged from 800 to 1000 J.days for the same three runs as in Fig. 1. The low-wavenumber region of $0 \leqslant m,n \leqslant 50$ is shown. Thick arrows represent the wavenumber n_β. Solid curves indicate the ''wave-turbulence boundary'' at which the reciprocal of the vorticity advection time is comparable to the Rossby-wave frequency.

is transferred as far as the lowest wavenumber of $n=2$. However, the energy flux around n_f becomes large as the forcing wavenumber increases, because the dissipation effect increases with an increase in n. For the experiments with rotation in group **B**, the energy flux function is parallel to that for no rotation in the energy-cascading range of $n_\beta \lesssim n \leqslant n_f$, indicating that the effect of rotation is weak in this range. Exceptions are #17–18 of large Ω/Ω_J; the energy flux function is slightly steeper than that for no rotation even in this energy-cascading range suggesting that the influence of rotation is large even in this range. In the range of $2 \leqslant n \lesssim n_\beta$, on the other hand, the energy flux function is not parallel to that of group **A** but it has a large decline; the energy transfer is largely suppressed in this range. For the runs in group **C**, the energy flux is smaller than that for no rotation in the range of $2 \leqslant n \lesssim n_f$; the upward energy cascade is strongly suppressed by the rotation even in the forcing range.

In contrast to the energy flux function, the enstrophy flux function is not constant at all even in the enstrophy-cascading range of $n \gtrsim n_f$ (not shown). This is mainly due to the form of the dissipation;[13] we did not use the hyperviscosity. For the experiments with rotation in group **B**, the enstrophy flux becomes large as the rotation rate increases. For the runs in group **C**, on the other hand, the enstrophy flux is smaller than that for no rotation in the range of $n \gtrsim n_f$ indicating that the normal enstrophy cascade is also strongly suppressed by the rotation.

Figure 4 shows the 2D energy spectral density $\overline{E}(m,n)$:

$$\overline{E}(m,n) = \frac{1}{2} \frac{n(n+1)}{a^2} \overline{|\psi_n^m(t)|^2}, \tag{7}$$

in the range of $n \leqslant 50$ for the same three runs as in Fig. 1. The energy density has the symmetry of $\overline{E}(-m,n) = \overline{E}(m,n)$ because $\psi \in \boldsymbol{R}$, so that it is shown only for $m \geqslant 0$. In the case of no rotation (a), the energy density increases by the upward energy cascade as the total wavenumber n decreases. The isopleths of $\overline{E}(m,n)$ are nearly independent of the zonal wavenumber m indicating that the flow field is homogeneous and isotropic as theoretically pointed out by Boer.[14] For the experiments with rotation (b)–(c), on the other hand, a large amount of energy is found around $m=0$ at the low wavenumbers of $n \lesssim n_\beta$ and the energy density $\overline{E}(m,n)$ decreases with an increase in m for fixed n. There is little energy in an airfoil-shaped region near the lower edge of the triangle, and this region becomes wide as the rotation rate increases (c). Here, the ''wave-turbulence boundary'' is introduced in the analogy of that in VM for the β-plane turbulence:

$$m = \frac{\overline{U}}{2\Omega a} n^2(n+1). \tag{8}$$

On this curve, the Rossby wave frequency $2\Omega m/\{n(n+1)\}$ is equal to the reciprocal of the vorticity advection time $\overline{U}n/a$. The curve expressed by Eq. (8) is also drawn in Figs. 4(b) and 4(c). The boundary of the airfoil-shaped region has a qualitatively similar shape to this curve, although these two curves quantitatively disagree.

Figures 4(b) and 4(c) show that the isopleths of $\overline{E}(m,n)$ are not horizontal even in the range of $n \gtrsim n_\beta$ but it has a gradual decline with m. Figure 5 also shows $\overline{E}(m,n)$ in the full wavenumber range for the other three runs of #1, #3, and #6 in series I with the forcing of small wavenumbers ($n_f=20$). In contrast to the runs in Fig. 4, these are chosen here to clarify the spectral anisotropy in the high-wavenumber region far away from the forcing. In the case of no rotation (a), the isopleths of $\overline{E}(m,n)$ are nearly independent of m, so that the flow field is homogeneous and isotropic in all the wavenumber ranges. For the experiments with rotation, on the other hand, the isopleths have a gradient with m even in the high-wavenumber region. When the rotation rate is large (c), the isopleths of $\overline{E}(m,n)$ are nearly vertical in this diagram and most of the energy is confined in the wavenumber region of $m \lesssim 50$ indicating a strong zonal anisotropy for all the range of n.

The energy distribution becomes zonally anisotropic owing to the effect of rotation and a large amount of energy

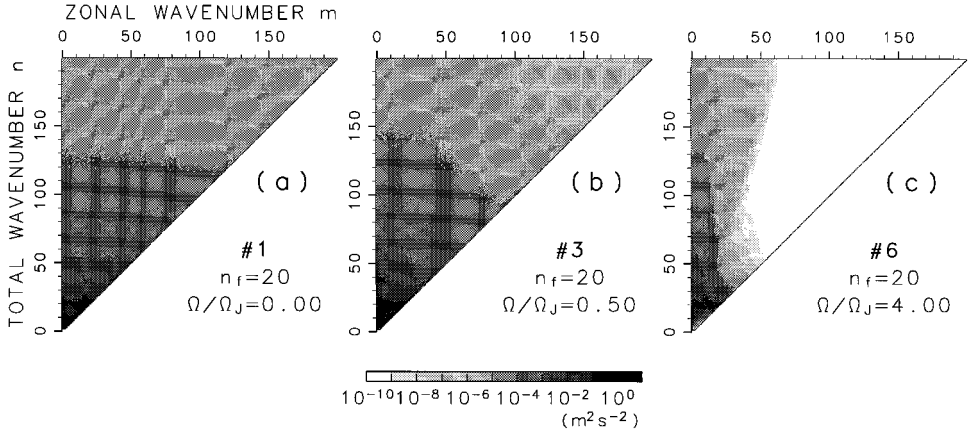

FIG. 5. Two-dimensional energy density averaged from 800 to 1000 J.days for three typical runs of (a) #1, (b) #3, and (c) #6 in series I. Full components are shown.

exists on the line of $m=0$. Thus the division of the energy spectrum $\overline{E(n)}$ into zonal-mean components $\overline{E_Z(n)}$ and disturbance components $\overline{E_D(n)}$ will be useful for summarizing the spectral anisotropy, where the two energy densities are defined as follows:

$$\overline{E_Z(n)}=\frac{1}{2}\frac{n(n+1)}{a^2}\overline{|\psi_n^0(t)|^2}, \tag{9}$$

$$\overline{E_D(n)}=\frac{1}{2}\sum_{\substack{m=-n\\ m\neq 0}}^{n}\frac{n(n+1)}{a^2}\overline{|\psi_n^m(t)|^2}. \tag{10}$$

Figure 6 shows $\overline{E_Z(n)}$ (solid line) and $\overline{E_D(n)}$ (short dashed line) for the same three runs as in Figs. 1 and 4. In the case without rotation (a), the disturbance energy density is dominant in all the wavenumbers. For the experiments with rotation (b)–(c), on the other hand, zonal-mean components become dominant in low wavenumbers. For the run in group **B**, $\overline{E_Z(n)}$ is comparable to or larger than $\overline{E_D(n)}$ in the range of $n\lesssim n_\beta$, indicating that the zonally symmetric flow field is dominant in this range. For the run in group **C**, the wavenumber range where $\overline{E_D(n)}\gtrsim\overline{E_Z(n)}$ extends toward the low-wavenumber range of $n\gtrsim 14$ beyond n_β.

B. Energy spectrum on a tangential plane

In this subsection, we compare local feature of the 2D turbulence in the spherical geometry with some numerical results obtained on a β-plane[5] by introducing a square tangential plane. A modified streamfunction field $\Psi(x,y,t)$ is defined and the 2D energy spectral density $E(k,l,t)$ is calculated from $\Psi(x,y,t)$ as shown in the Appendix, where x and y are the abscissa and ordinate of the plane, respectively, and k and l are x- and y-wavenumbers, respectively.

Figure 7 shows the time-averaged 2D energy density $\overline{E(k,l)}$ for the run #7 without rotation (group **A**). Twenty-five energy densities for each plane are also averaged. The energy density $\overline{E(k,l)}$ roughly shows a homogeneous and isotropic distribution, although the effect of the aliasing error remains around the lines $k=0$ and $l=0$.

The modified streamfunction fields $\Psi(x,y,t)$ at $t=1000$ J.days are shown in Figs. 8(a)–8(c) for the run #10 with moderate rotation rate ($\Omega/\Omega_J=1.00$; group **B**). On equatorial and middle-latitude tangential planes (a)–(b), the zonal band structure is dominant, although the bands have a little curvature in middle latitudes (b). On the other hand, a coaxial circular structure dominates on a polar tangential plane (c). Figures 8(d)–8(f) show the 2D energy density

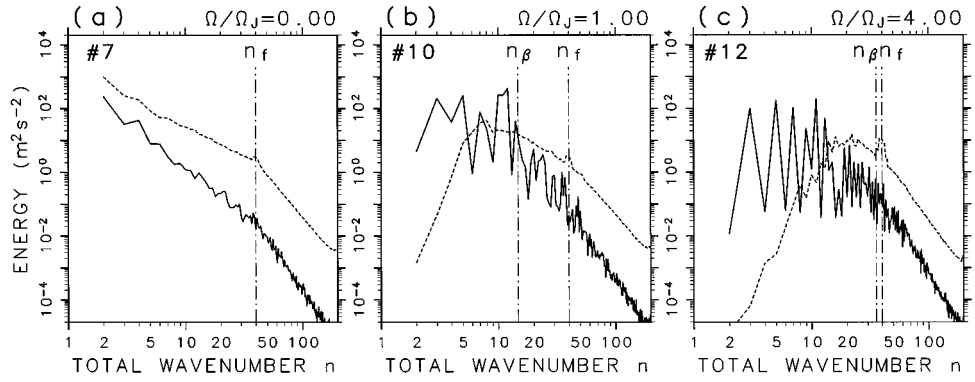

FIG. 6. Energy density for zonal components (solid line) and that for disturbance components (dotted line) averaged from 800 to 1000 J.days for the same three runs as in Figs. 1 and 4. Thin dot-dashed lines represent the wavenumbers n_f and n_β.

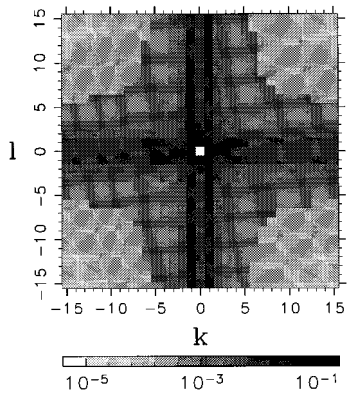

FIG. 7. Two-dimensional energy density calculated from the modified streamfunction field for run #7. Time averages from 800 to 1000 J.days and ensemble averages of 25 cases of the tangential planes.

$\overline{E}(k,l)$ for this run. In the tangential planes in low and middle latitudes (d)–(e), the energy distribution is rather anisotropic owing to the ''β-effect''; the energy around $k=0$ is large and the isopleths of $\overline{E}(k,l)$ are elongated in the direction of the l-axis. The energy density is large on the horizontal lines of $l=\pm 1$ nearly independently of the wavenumber k. The difference of the spectral anisotropy is not very significant between the equatorial region (d) and middle latitudes (e). In the polar tangential planes (f), on the other hand, the distribution of the energy is isotropic except for the aliasing. This isotropic distribution of $\overline{E}(k,l)$ is rather different from that for #7 without rotation (Fig. 7); the energy is confined into the lower-wavenumber region.

The energy density $\overline{E}(k,l)$ for the run #12 with large rotation rate ($\Omega/\Omega_J=4.00$; group **C**) is shown in Fig. 9. The spectral anisotropy is evident in the equatorial region (a) and the energy density $\overline{E}(k,l)$ shows a clear dumbbell shape at the low-wavenumber region. The dumbbell shape reminds us of the original finding by VM in their β-plane experiment. The energy has a maximum at relatively large meridional wavenumbers around $l=\pm 5$ corresponding to the zonal band structure in the streamfunction field (not shown). Similar spectral anisotropy is obtained in middle latitudes (b) except for the dumbbell shape. Figure 10 also shows the energy density $\overline{E}(k,l)$ for the run #18 with a large rotation rate ($\Omega/\Omega_J=4.00$; group **B**) and $n_f=79$. The isopleths are elongated in the l-axis and the energy is accumulated around $k=0$ in middle and low latitudes (a)–(b). Some accumulations around the lines of $l=\pm 2$ are also seen. A similar dumbbell structure can be identified in the equatorial region (a) and a hint of it in middle latitudes (b).

IV. DISCUSSION

For the 2D turbulence with the effect of differential rotation, Maltrud and Vallis[6] have already studied the energy transfer in their numerical experiments on a β-plane, and showed that the transferred energy accumulates around k_β and that the power law in the energy-cascading range remains nearly proportional to $k^{-5/3}$. Although the wavenumber n_β we used is not identical to k_β, these features of the energy spectrum influenced by the rotation are obtained in our spherical experiments in group **B** with small and moderate rotation rates (Fig. 2). For the cases with a larger rotation

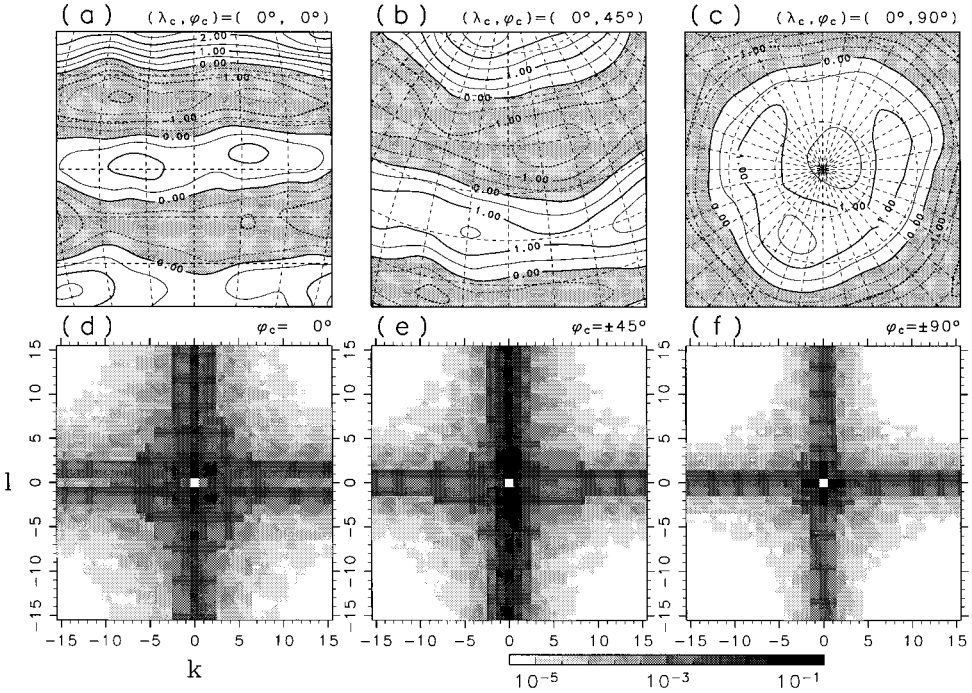

FIG. 8. (a)–(c) Modified streamfunction field $\Psi(x,y,t)$ at $t=1000$ J.days for run #10. The center of the tangential plane (λ_c,φ_c) is indicated on the top of each figure. Meridians and parallels are drawn for every 10°. The contour interval is 5×10^{-1} and negative areas are shaded. (d)–(f) The two-dimensional energy density calculated from the modified streamfunction field for run #10. The number in the upper right of each figure represents the central latitude φ_c of the tangential plane. Time averages from 800 to 1000 J.days and ensemble averages of (d) 9 cases, (e) 12 cases, and (f) 4 cases.

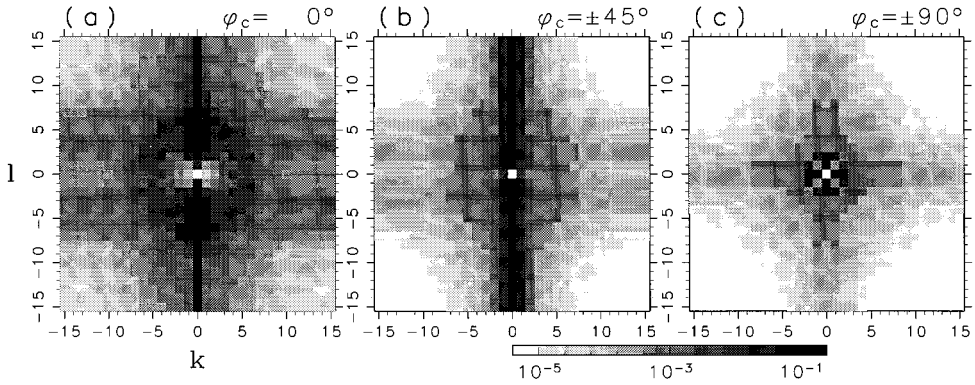

FIG. 9. The same as in Figs. 8(d)–8(f) but for run #12.

rate ($\Omega/\Omega_J \geqslant 2.00$) in group **B**, the energy cascade is largely influenced by the rotation, so that the energy is dissipated faster in the energy-cascading range. Hence the energy spectrum in this range becomes steeper than $n^{-5/3}$ as shown in Fig. 2 (#11, #17, and #18). For the experiments in group **C**, on the other hand, the upward energy cascade is largely inhibited by the rotation as shown in Fig. 3. The enstrophy cascade is also suppressed because the normal enstrophy cascade is strongly connected with the upward energy cascade. Thus the energy spectrum in group **C** is steeper than n^{-4} in the enstrophy-cascading range.

The spherical analog of the ''wave-turbulence boundary'' introduced by VM exhibits a characteristic airfoil shape near the lower edge of the triangular wavenumber space [Figs. 4(b) and 4(c)], and there is little energy in a qualitatively similar airfoil-shaped region. However, the boundary largely overpredicts the outline of the energy distribution as seen in Fig. 4(c) in contrast with the case on a β-plane.[5] Some modification of the ''wave-turbulence boundary'' is necessary for the spherical geometry. The vertically integrated kinetic energy spectrum of the real atmosphere obtained by Boer and Shepherd[15] also shows a similar airfoil-shaped region in which little energy exists at the low-wavenumber region of $m,n \lesssim 5$. This correspondence suggests the two-dimensional Rossby-wave/turbulence nature of the large-scale atmospheric motion.

The spectral anisotropy is also found in the high-wavenumber region of the triangular wavenumber space [Figs. 5(b) and 5(c)]; the energy density decreases with an increase in the zonal wavenumber m. This tendency of the zonal anisotropy in high wavenumbers was already obtained by Holloway and Hendershott[7] and Basdevant *et al.*[8] in their experiments on β-planes. Thus the spectral anisotropy in the zonal direction is a common feature of the 2D turbulence on a rotating sphere and on a β-plane. It is necessary to investigate the reason why the energy density distributes anisotropically even in the high-wavenumber region where the effect of rotation is very small.

When the flow field is projected on an equatorial tangential plane, the 2D energy density shows a clear dumbbell shape in the low-wavenumber region as in VM for the runs with a large rotation rate [Figs. 9(a) and 10(a)]. The wavenumber k_β estimated for the equatorial tangential plane with the value of β at the equator (the second last column in Table I) is somewhat larger than the wavenumber of the boundary on the k-axis, and this tendency of overprediction is also obtained by VM. For the flow fields projected on middle-latitude tangential planes, on the other hand, the 2D energy density does not show such a clear dumbbell shape even in the runs with large rotation rates [Figs. 9(b) and 10(b)]. In these cases, zonal bands in the modified stream-function field has a little curvature, particularly in higher latitudes [Fig. 8(b)]. Furthermore, the β-plane approximation is not so good due to the large size of the tangential plane. Thus the energy density may not exhibit a clear dumbbell shape. Reduction of the size of the tangential plane will be

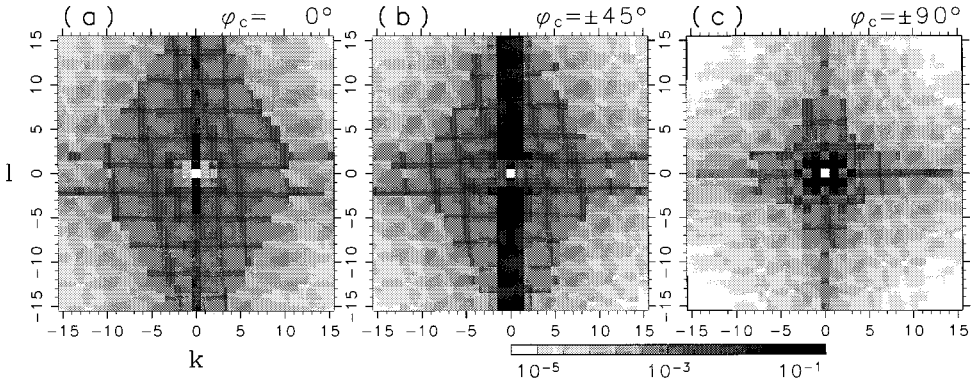

FIG. 10. The same as in Figs. 8(d)–8(f) but for run #18.

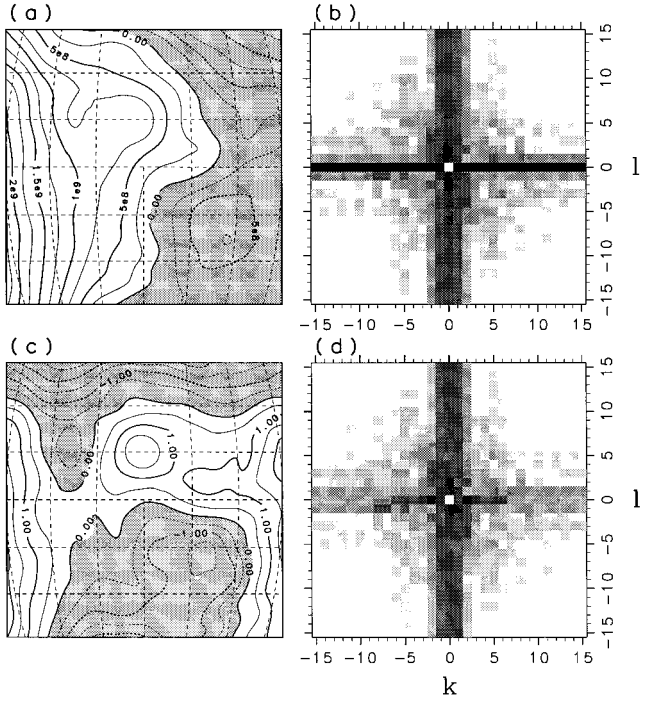

FIG. 11. (a) Streamfunction field $\psi(x',y',t)$ at $t=1000$ J.days for run #7. The streamfunction is orthographically projected on an equatorial tangential plane. Meridians and parallels are drawn for every 10°. A contour interval is 2.5×10^{8} m^2 s^{-1} and negative areas are shaded. (b) The two-dimensional energy density calculated from the streamfunction field $\psi(x',y',t)$ in (a). Dark shades indicate high values of the energy. (c) The modified streamfunction field $\Psi(x,y,t)$ obtained from the streamfunction $\psi(x',y',t)$ shown in (a). See the text for a definition. The contour interval is 5×10^{-1} and negative areas are shaded. (d) The two-dimensional energy density calculated from the modified streamfunction field $\Psi(x,y,t)$ in (c). Shading is done by means of multiplying a factor to the color code in (b).

necessary to get a clear dumbbell shape, although it requires very hard computations with a high-resolution spherical model.

V. CONCLUSIONS

The datasets on the forced 2D turbulence on a rotating sphere which were obtained in our recent numerical experiments with a high-resolution barotropic model were analyzed to study the spectral anisotropy due to the rotation of sphere. The energy spectral density is calculated not only in the full spherical domain but also in some local tangential planes to compare the results with that obtained in the previous β-plane experiments for the assessment of the β-plane approximation.

For the runs without rotation (we called group **A**), the energy is transferred to the lowest wavenumber of $n=2$. For the runs of group **B** with rotation, on the other hand, the upward energy cascade ceases around a characteristic wavenumber n_β at which the linear ''β-term'' due to the planetary rotation is comparable to the nonlinear Jacobian term, and the transferred energy accumulates in the range of $n \lesssim n_\beta$, where the energy density of zonal components is dominant. As the rotation rate increases, the energy-cascading range becomes narrow, although the slope in this range remains close to $n^{-5/3}$. When the wavenumber n_β is nearly equal to or larger than the forcing wavenumber n_f (group **C**), the upward energy cascade is strongly inhibited by the effect of rotation.

The 2D energy density in the spherical domain exhibits the isopleths independent of the zonal wavenumber m for the runs without rotation, indicating that the flow field is homogeneous and isotropic. In the case with rotation, on the other hand, a large amount of energy is in the range of $2\leqslant n \lesssim n_\beta$ with $m=0$, while little energy is found in a characteristic airfoil-shaped region near the lower edge of the triangular wavenumber space. The airfoil-shaped region becomes wide as the rotation rate increases. The 2D energy density in the high-wavenumber region also shows anisotropic distribution as well as in the low-wavenumber region; most of the energy is confined in the lower zonal wavenumbers for all the range of n. The confinement becomes more evident as the rotation rate increases.

For some experiments, the flow field in the spherical geometry was projected orthographically on some tangential planes to compare the energy density distributions in 2D wavenumber space with those obtained in some β-plane experiments. In the case without rotation, the 2D energy density shows the homogeneous and isotropic distribution. For the runs with rotation, on the other hand, the distribution of the 2D energy density largely depends on the value of β at the center of the plane. In the equatorial tangential planes, the 2D energy density shows anisotropic distribution. The isopleths are elongated elliptically in the direction of the meridional wavenumber, and the energy is accumulated within small zonal wavenumbers. There are other accumulations along constant meridional wavenumbers due to the emergence of a zonal band structure in the flow field. The 2D distribution in low wavenumbers shows the characteristic dumbbell shape of little energy density as shown in Vallis and Maltrud.[5] Similar anisotropic features are obtained in the middle-latitude tangential planes except for the dumbbell shape in the low-wavenumber region. In the polar tangential planes the distribution of 2D energy density is isotropic, because the circumpolar vortex dominates over the plane.

ACKNOWLEDGMENTS

GFD-DENNOU Library was used for drawing the figures. This work was supported in part by the Grant-in-Aid from the Ministry of Education, Science, Sports and Culture of Japan, and by the Grant-in-Aid for the Cooperative Research with the Center for Climate System Research, University of Tokyo. Computations were done in part on the KDK system at Radio Atmospheric Science Center, Kyoto University.

APPENDIX: DEFINITION OF THE MODIFIED STREAMFUNCTION ON A TANGENTIAL PLANE

The streamfunction field on the sphere is orthographically projected on a square tangential plane which is in contact with the sphere at a point (λ_c,φ_c) and has sides of a (the radius of the sphere). We select twenty-five tangential planes to cover all around the sphere considering the ratio of areas: nine planes in the equatorial region ($\varphi_c=0°$) with an

equal longitudinal difference of $\Delta\lambda_c=40°$, twelve in the middle latitudes ($\varphi_c=\pm 45°$) with $\Delta\lambda_c=60°$, and four in the polar regions ($\varphi_c=\pm 90°$) with two different orientations (45°) for each pole. As an example, the streamfunction field $\psi(x',y',t)$ on an equatorial tangential plane at $t=1000$ J.days is shown in Fig. 11(a) for run #7, where x' and y' are the abscissa and ordinate of the plane, respectively. Figure 11(b) shows 2D energy spectral density calculated from this streamfunction field shown in Fig. 11(a):

$$E_O(k,l,t)=\left(\frac{2\pi}{a}\right)^2\frac{k^2+l^2}{2}|\hat{\psi}_l^k(t)|^2, \tag{A1}$$

where k and l are x'- and y'-wavenumbers, respectively, and $\hat{\psi}_l^k(t)$ is an expansion coefficient of the Fourier transformation of $\psi(x',y',t)$:

$$\hat{\psi}_l^k(t)=\int_0^a\int_0^a \psi(x',y',t)e^{-i(2\pi/a)(kx'+ly')}dx'dy'. \tag{A2}$$

The number of grid points in the x'-direction I and that in the y'-direction J are set to $I=J=96$ considering the resolution of the spherical model, so that the truncation wavenumber is 48. For this resolution, the forcing wavenumbers $n_f=20$, 40, and 79 on the sphere roughly correspond to the wavenumbers $\kappa_f=\sqrt{k_f^2+l_f^2}=3$, 6, and 12, respectively. As shown in Fig. 11(b), discontinuity of $\psi(x',y',t)$ at the boundaries brings an aliasing error to the spectrum, especially around the lines $k=0$ and $l=0$.

To reduce the effect of the discontinuity, a modified streamfunction $\Psi(x,y,t)$ is defined as follows:

$$\Psi(x,y,t)=\frac{\psi(x',y',t)-\psi_r(x',y',t)}{\sqrt{\langle\langle\{\psi(x',y',t)-\psi_r(x',y',t)\}^2\rangle\rangle}}, \tag{A3}$$

$$x=\frac{2\pi}{a}x', \quad y=\frac{2\pi}{a}y', \tag{A4}$$

where $\psi_r(x',y',t)=\alpha x'+\beta y'+\gamma$ is a regression plane obtained from the streamfunction $\psi(x',y',t)$; α,β, and γ are determined by the least squared method:

$$\begin{pmatrix}\alpha\\ \beta\\ \gamma\end{pmatrix}=\begin{pmatrix} J\sum_{i=0}^{I-1}(x_i')^2 & \sum_{i=0}^{I-1}\sum_{j=0}^{J-1}x_i'y_j' & J\sum_{i=0}^{I-1}x_i' \\ \sum_{i=0}^{I-1}\sum_{j=0}^{J-1}x_i'y_j' & I\sum_{j=0}^{J-1}(y_j')^2 & I\sum_{j=0}^{J-1}y_j' \\ J\sum_{i=0}^{I-1}x_i' & I\sum_{j=0}^{J-1}y_j' & IJ \end{pmatrix}^{-1} \times\begin{pmatrix}\sum_{i=0}^{I-1}\sum_{j=0}^{J-1}x_i'\psi(x_i',y_j',t)\\ \sum_{i=0}^{I-1}\sum_{j=0}^{J-1}y_j'\psi(x_i',y_j',t)\\ \sum_{i=0}^{I-1}\sum_{j=0}^{J-1}\psi(x_i',y_j',t)\end{pmatrix}, \tag{A5}$$

$$x_i'=\frac{a}{I}i \quad (i=0,1,2,\cdots,I-1),$$

$$y_j'=\frac{a}{J}j \quad (j=0,1,2,\cdots,J-1).$$

A bracket $\langle\langle\cdots\rangle\rangle$ in Eq. (A3) indicates an area average on the tangential plane. The modified streamfunction field $\Psi(x,y,t)$ exhibits a normalized deviation of $\psi(x',y',t)$ from the regression plane $\psi_r(x',y',t)$. Note that the sides of the tangential plane are normalized to 2π by Eq. (A4). Figure 11(c) shows the modified streamfunction field $\Psi(x,y,t)$ obtained from the streamfunction field shown in Fig. 11(a). The pattern of $\Psi(x,y,t)$ does not closely resemble that of the original. However, the spectral coefficients of the regression plane $\psi_r(x',y',t)$ are equal to zero except for the case $kl=0$. Hence the modified streamfunction preserves the statistical properties of the original streamfunction. Figure 11(d) shows the 2D energy spectral density calculated from $\Psi(x,y,t)$ shown in Fig. 11(c):

$$E(k,l,t)=\frac{k^2+l^2}{2}|\hat{\Psi}_l^k(t)|^2, \tag{A6}$$

where $\hat{\Psi}_l^k(t)$ is an expansion coefficient of Fourier transformation of $\Psi(x,y,t)$:

$$\hat{\Psi}_l^k(t)=\int_0^{2\pi}\int_0^{2\pi}\Psi(x,y,t)e^{-i(kx+ly)}dxdy. \tag{A7}$$

Obviously, the distribution of $E(k,l,t)$ does not differ from that of $E_O(k,l,t)$ except for the lines $k=0$ and $l=0$.

[1] R. H. Kraichnan, ''Inertial ranges in two-dimensional turbulence,'' Phys. Fluids **10**, 1417 (1967).
[2] C. E. Leith, ''Diffusion approximation for two-dimensional turbulence,'' Phys. Fluids **11**, 671 (1968).
[3] G. K. Batchelon, ''Computation of the energy spectrum in homogeneous two-dimensional turbulence,'' Phys. Fluids **12**, 233 (1969).
[4] P. B. Rhines, ''Waves and turbulence on a beta-plane,'' J. Fluid Mech. **69**, 417 (1975).
[5] G. K. Vallis and M. E. Maltrud, ''Generation of mean flows and jets on a beta plane and over topography,'' J. Phys. Oceanogr. **23**, 1346 (1993).
[6] M. E. Maltrud and G. K. Vallis, ''Energy spectra and coherent structures in forced two-dimensional and beta-plane turbulence,'' J. Fluid Mech. **228**, 321 (1991).
[7] G. Holloway and M. Hendershott, ''Stochastic closure for nonlinear Rossby waves,'' J. Fluid Mech. **82**, 747 (1977).
[8] C. Basdevant, B. Legras, R. Sadourny, and M. Beland, ''A study of barotropic model flows: Intermittency, waves, and predictability,'' J. Atmos. Sci. **38**, 2305 (1981).
[9] T. G. Shepherd, ''Rossby waves and two-dimensional turbulence in a large-scale zonal jet,'' J. Fluid Mech. **183**, 467 (1987).
[10] T. Nozawa and S. Yoden, ''Formation of zonal band structure in forced two-dimensional turbulence on a rotating sphere,'' Phys. Fluids **9**, 2081 (1997).
[11] G. P. Williams, ''Planetary circulations: 1. Barotropic representation of Jovian and terrestrial turbulence,'' J. Atmos. Sci. **35**, 1399 (1978).
[12] S. Yoden and M. Yamada, ''A numerical experiment on two-dimensional decaying turbulence on a rotating sphere,'' J. Atmos. Sci. **50**, 631 (1993).
[13] J. Y.-K. Cho and L. M. Polvani, ''The emergence of jets and vortices in freely evolving, shallow-water turbulence on a sphere,'' Phys. Fluids **8**, 1531 (1996).
[14] G. J. Boer, ''Homogeneous and isotropic turbulence on the sphere,'' J. Atmos. Sci. **40**, 154 (1983).
[15] G. J. Boer and T. G. Shepherd, ''Large-scale two-dimensional turbulence in the atmosphere,'' J. Atmos. Sci. **40**, 164 (1983).